

## Role of smile correction in mineral detection on hyperion data

M. Mohammady Oskouei\* and S. Babakan

*Faculty of Mining Engineering, Sahand University of Technology, Tabriz, Iran*

Received 14 October 2015; received in revised form 1 January 2016; accepted 11 January 2016

\*Corresponding author: mohammady@sut.ac.ir (M. Mohammady Oskouei).

### Abstract

This work aims to extract the mineralogical constituents of the Lahroud Hyperion scene situated in the NW of Iran. Like the other push-broom sensors, Hyperion images suffer from spectral distortions, namely the smile effect. The corresponding spectral curvature is defined as an across-track wavelength shift from the nominal central wavelength, and alters the pixel spectra. The common “column mean adjusted in MNF space” method was employed in this work to improve the processing accuracy by minimizing the smile effect before carrying out the atmospheric and topographical corrections. The mineral distributions were mapped by applying the standardized hyperspectral processing methodology developed by analytical imaging and geophysics (AIG). The spectral unmixing of the data resulted in the identification of five indicative minerals including natrolite, opal, analcime, kaolinite, and albite; and their spectra were employed for the generation of their distribution maps. Comparison of the results of the data processing with and without smile correction indicated a better classification performance after the smile correction. Quantitative validation of the final mineralogical map was performed using the 100 k geological map and reports of the region. Therefore, the coverage of the extracted minerals were investigated regarding the location of the lithological units in ArcGIS that implies a high coincidence. The mineral distributions in the final map show a high consistency with the geological map of the studied area, and thus it could be utilized successfully to reveal the mineralization trend in the region.

**Keywords:** *Hyperion Data, Standardized Hyperspectral Processing Methodology, Smile Correction, Mineralogical Mapping.*

### 1. Introduction

Hyperspectral sensors provide a complete spectral pattern for the superficial features that can be utilized for target detection, and discrimination and classification in wide branches of sciences such as the geological studies and mineral exploration [1, 2]. In contrast to the multispectral sensors, the hyperspectral sensors significantly improve the achievable spectral details of the materials present on the earth. Thus they have been utilized successfully in the mineralogical mapping due to their higher spectral resolution [2].

“Mixed pixels” is a challenging problem in hyperspectral remote sensing, which arises from their low spatial resolution. Finding pure pixels consisting solely of one mineral is, therefore,

impossible. The measured radiance in a mixed pixel reflects the spectral characteristics of a combination of existing minerals, and needs to identify sub-pixel materials before classification [1, 3]. On the other hand, a suitable pre-processing and corrections are required to achieve accurate outcomes since they will rectify the data errors or the undesired elements present on the scene [4, 5].

Hyperion data exhibits a wavelength shift in the across-track direction from the central wavelength of the bands in columns known as the spectral smile or frown effect. This effect is characteristic of the push-broom sensors, and depends on the wavelength and position of the image pixel column. The smile effect is most clearly evident

in the visible near-infrared (VNIR) bands in contrast to the short wave infrared (SWIR) range [6]. This small variation might be important in the case of identification of the minerals by affecting their diagnostic absorption features [7].

There are various smile correction methods in use but the common column mean adjusted in MNF space method was applied in this research work before carrying out the atmospheric and topographic corrections. A mineral distribution map was then generated through the standardized hyperspectral processing methodology developed by analytical imaging and geophysics (AIG). In addition, a similar processing was conducted on the data without smile corrections to evaluate the effect of the corrections.

The results obtained were validated using the corresponding 100 k geological map of the studied area regarding the previously determined mineralogical composites of each alteration zone. The coverage of the extracted minerals in the lithological units was determined in ArcGIS, which implies the high consistency with the distribution of the detected minerals.

## 2. Study area

The studied area is located at 21.6 km NW of Lahroud in Ardabil province between the 47°33'18.6" and 47°36'31.6" N latitudes and the 38°34'55" and 38°30'21.7" E longitudes, covering approximately 46.47 km<sup>2</sup> of the area. This area is part of the Lahroud 1:100,000 geological map. It is situated in the Alborz-Azerbaijan structural zone. Three main alteration zones are exposed to the Lahroud sheet including the alunitized, kaolinitized, and silicified zones, which cover 56.3% of the studied area. Altered rocks are the most extended lithological units in this area. Meanwhile, a small portion of this region (~7%) is covered by sediments.

## 3. Hyperion

Hyperion is a hyperspectral instrument on the earth-observing 1 (EO-1) spacecraft, and records the electromagnetic energy across the wavelength range of 0.4-2.5  $\mu\text{m}$  in 242 continuous spectral bands with a ~10 nm spectral bandwidth and a 30 m ground resolution. Hyperion acquires data via two spectrometers (VNIR (0.4-1  $\mu\text{m}$ ) and SWIR (0.9-2.5  $\mu\text{m}$ )) [8]. Surface minerals have diagnostic spectral signatures in this spectral range, enabling them to be detected using the remote sensing analysis techniques [8]. Thus processing high spectral resolution images will facilitate the discrimination of the earth-surface materials. These characteristics are generally

utilized for identification of the indicator alteration minerals as a direct evidence of the existing mineralization [2].

However, Hyperion is a push-broom type sensor with poorly calibrated detectors indicating numerous problems in the VNIR/SWIR regions such as the vertical strips and smile effect. Correction of these effects will improve the accuracy of the extracted features and the resulting unmixing and classification map [2].

## 4. Pre-processing

Generally, the remotely sensed data contains flaws or deficiencies in their raw form. Removal or rectification of the errors and unwanted elements is termed as pre-processing since they are commonly carried out before the "information extracting" (processing) tasks [5].

Pre-processing is necessary to provide high-quality data for analysis [9, 10]. Sun azimuth, elevation, and sensor response influence the observed energy [11]. Therefore, in order to obtain the real irradiance or reflectance, those radiometric distortions must be corrected. Since the Hyperion data for the studied area is level 1R, the radiometric correction has already been performed by the distributor.

### 4.1. Smile effect

A common error, obvious in push-broom sensors, is referred to as the spectral smile, also known as the spectral curvature or frown effect. It is a kind of spectral distortion arising from a change in the depression angle related to the field position. Smile effect is defined as a wavelength shift in the spectral domain from the nominal central wavelength, depending on the across-track pixel (column) position in the swath. The central wavelength of the bands varies with the spatial position across the image width in a smoothly curving pattern. Very often the peak of this smooth curve tends to be in the middle of the image, providing a shape of a smile or frown that alters the pixel spectra. Therefore, the extracted information from a smiled Hyperion image will most likely reduce the subtle surface classification accuracies [4].

The spectral smile has been reported to vary from 2.6 to 3.6 nm in VNIR and ~1 nm in the SWIR range that affects the diagnostic absorption features of the minerals [12]. As the bandwidth of Hyperion is about 10 nm, such a little wavelength shift seems not to be a serious problem, although in the case of mineral identification, this small variation is important [7].

### 4.1.1. Smile indicators

The smile effect is not identifiable through the individual Hyperion bands. Indicators are, therefore, utilized to determine whether a Hyperion image suffers from the smile problem. Two indicators have been suggested for this purpose including the MNF transformation and the band difference technique [2, 13].

#### 4.1.1.1. MNF

Images significantly suffering from the smile effect present a brightness gradient or variation in the MNF space (normally, at the first MNF band) [2, 4, 13, 14]. Accordingly, a forward MNF rotation was separately applied to VNIR (8-57) and SWIR (79-224) of the data. The first components of the resulting MNF images (MNF1) for each spectrometer in addition to the horizontal profile for the same line (line 3 of the Hyperion image) of the image are illustrated in Figure 1.

According to the resultant images in Figure 1, there is an obvious brightness gradient in the MNF1 image of the VNIR bands causing a frown shape on the across-track pixel reflectance. In the SWIR region, however, the gradient is negligible, and there are only random variations in the respected profile.

### 4.1.1.2. Band difference images

An alternative method used to survey the smile effect is the application of the absorption features (AFs) of gases (e.g. O<sub>2</sub> and CO<sub>2</sub>). The smile effect results in a brightness gradient after calculation of the difference images of the bands affected from these absorption features [13]. Oxygen has a strong AF on the 762 nm wavelength (Hyperion band 41), also affecting the bands 40 and 42. It is expected that oxygen would contribute equally to all pixels of the image in the mentioned bands if the spectral smile did not affect the image significantly. Thus the subtraction image of the bands around this absorption feature (bands 40 and 42) should result in an image with zero values across the track direction [13, 15]. In the same way, CO<sub>2</sub> has a distinct absorption feature on the 2 μm wavelength, and is then helpful for a SWIR spectrometer [16]. The difference images obtained using the mentioned approach are illustrated in Figure 2. The outcome is the same as the MNF method that implies the obvious gradient in the VNIR range. Evaluation of the across track profile of this image also demonstrated the non-linearity variation indicating the existence of a significant smile effect in the VNIR region of the dataset.

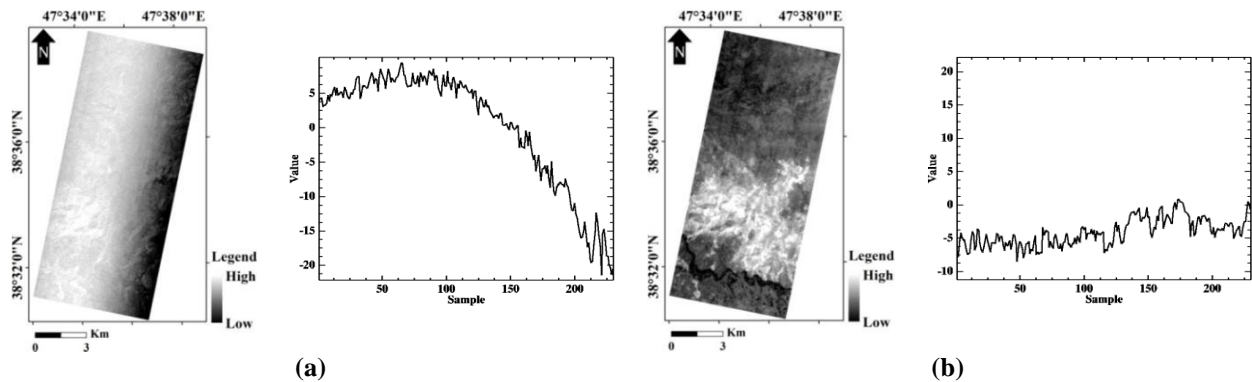


Figure 1. MNF1 indicator images of smile effect and corresponding across-track pixel reflectance variations for VNIR (a) and SWIR (b) spectrometers.

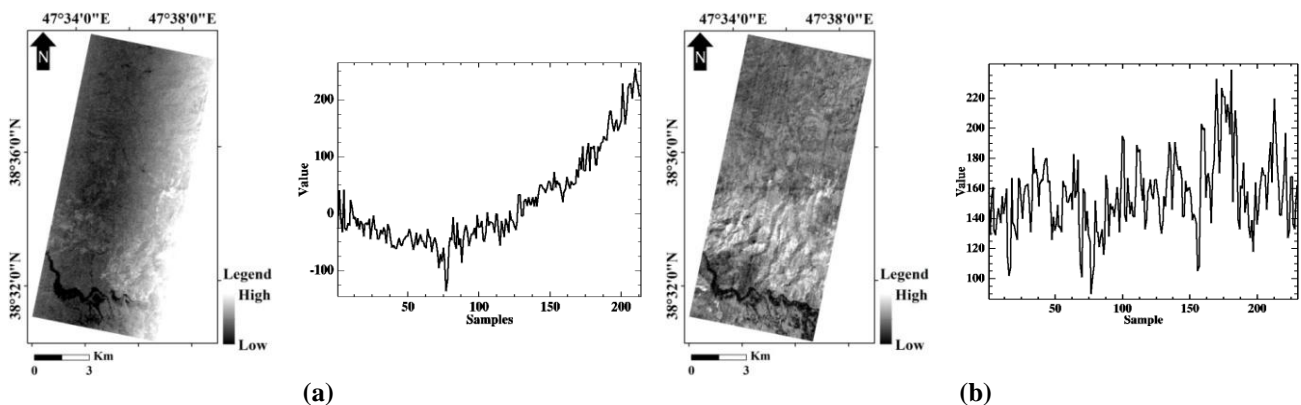


Figure 2. Band difference indicator images of smile effect and corresponding across-track pixel reflectance variations in (a) VNIR region (band 40-band 42), and (b) SWIR region (band 184-band 186).

### 4.1.2. Smile correction

The VNIR bands of Hyperion significantly suffers from smile effect, as demonstrated in the previous section. Despite the high spectral resolution of the Hyperion images, these small shifts alter the pixel spectra so that it could reduce the classification accuracies in mineral mapping. There are various methods developed for this correction, although none of them has been widely accepted by the researchers yet. The most common approaches are as follow [4]:

I- Moving linear fitting and interpolation that cannot remove the smile effect on the Hyperion images completely. It can be clarified through the possible post-launch variations in the spectral calibration.

II- Column mean adjusted in radiance space that replaces the column mean values of the original bands by the corresponding band mean values. This method creates false spectra, assuming the sufficient homogeneity of the image (not generally true). Nevertheless, this approach removes the brightness gradient.

III- Column mean adjusted in MNF space that replaces the column mean values with the corresponding band mean values in MNF space. Similarly, this method also removes the brightness gradient created false spectra.

A reliable smile correction is able to remove the brightness gradient in the indicator images, and must retain the spectral fidelity after correction (would not create false spectral features). According to Goodenough et al. [4], the aforementioned approaches maintain the basic spectral absorption features but do not remove the smile effect completely. The first one is not applicable here as the pre-launch and post-launch calibrations are different and the column mean adjusting method generates false spectra (artifacts) that are different from the original Hyperion data [4].

The column mean adjusted in MNF space method was, therefore, utilized in this work by programming in MATLAB. To perform this task, the column mean value of the MNF bands were set to the global band mean values, and then the processed dataset was rotated back into the radiance space. The results on MNF1 and band differential indicator images after the correction were illustrated in Figure 3. This figure implies elimination of the brightness gradient in both of the indicator images. The across-track pixel reflectance variation does not demonstrate the smile effect as well.

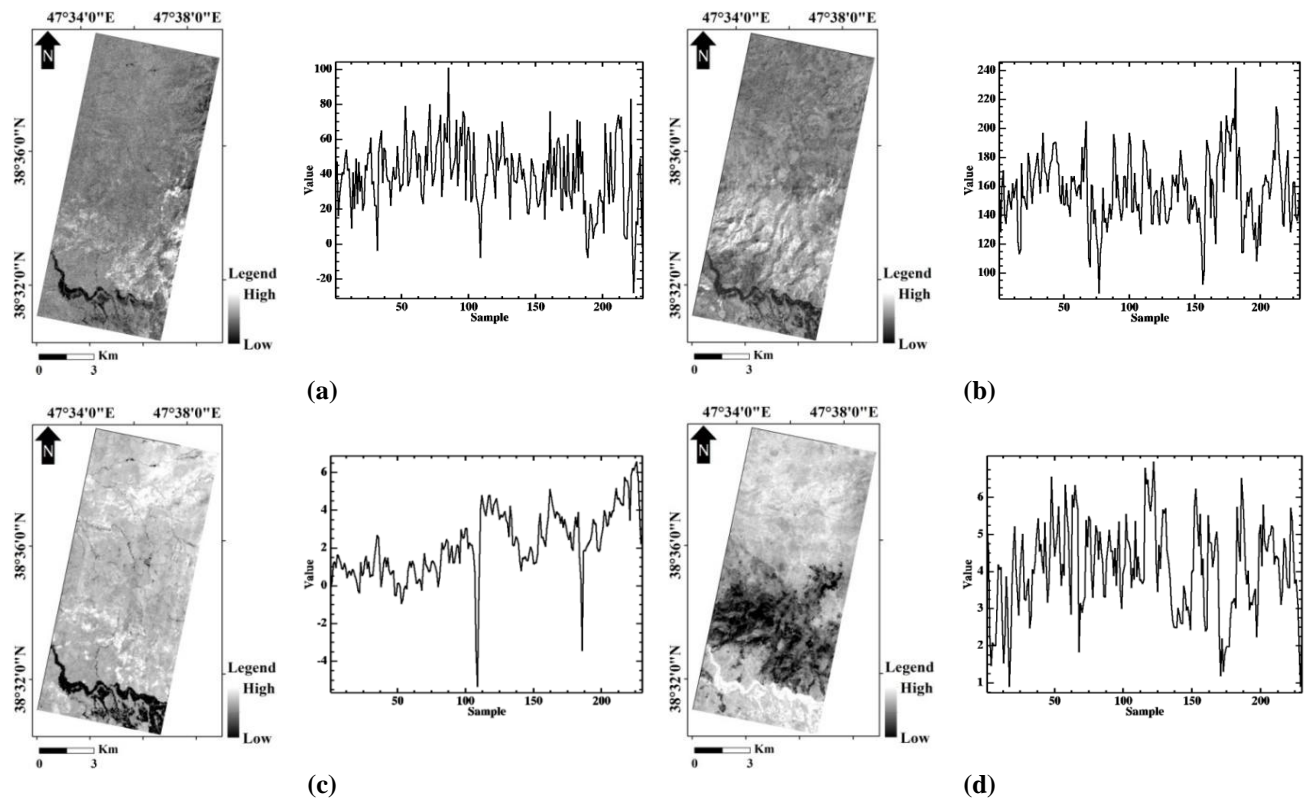


Figure 3. Smile indicator images of de-smiled Hyperion dataset and corresponding horizontal profiles, band differential image of a) VNIR bands (B40-B42), and b) SWIR bands (B184-B186); MNF1 of a) VNIR (bands 8-57), and d) SWIR (bands 79-224).

## 4.2. Atmospheric correction

The atmospheric correction aims to remove the influence of the atmosphere on recorded energy. It separates the contribution of earth responses from the atmosphere-land mixed signals. In fact, sunlight in the way of the sun to the earth and from the earth to the sensor is scattered by various constituents of the atmosphere. Therefore, the actual reflectance of the earth features have to be accurately recovered to provide a more successful classification and discrimination performance. Atmospheric correction is the premise of many quantitative algorithms for extraction of the informative signals from data [17-20].

In this study, the atmospheric correction was performed using the FLAASH (fast line-of-sight atmospheric analysis of spectral hypercube) algorithm. FLAASH is a MODTRAN4-based atmospheric correction software package that provides accurate and physical derivation of the apparent surface reflectance. It extracts some of the necessary parameters from the data, and compares the image radiance spectra with the MODTRAN lookup tables on a pixel-by-pixel basis to determine the scaled surface reflectance [18, 21].

## 4.3. Topographic correction

Topography seriously affects the quality of the remotely sensed data since it alters the viewing angle for each pixel on the scene. Therefore, it is a vital correction for remotely sensed data, especially in rugged terrain [22-24]. The sun facing a slope presents higher reflectance values than its opposite side, and this will cause a possible misclassification of similar ground features in different topographies. Different techniques have been developed to reduce topographical distortions employing the digital elevation model (DEM). Efficient removal or minimization of the terrain-dependent illumination is substantial in rugged terrains to extract the maximum and accurate information [23].

The topographic correction techniques are categorized into two main groups: Lambertian approaches that assumes uniform/equal reflection of the incident solar energy by surface in all directions and attempts to reduce only the distortions caused by the surface orientation; and non-Lambertian algorithms that models diffused irradiance by constant values depending on both the land cover type and bands wavelengths [23, 25-29]. The impact of the topographic illumination is mainly depended on the

wavelength of the incoming radiation, the local solar incidence angle, and the specific reflectance characteristics of the land cover types [30, 31].

The cosine method is one of the Lambertian approaches. When  $L_H$  and  $L_T$  denote the radiance observed over the corrected and inclined (before correction) surfaces respectively; and  $\theta_z$  and  $\theta_i$  are the solar zenith angle and incident angle, the cosine correction for topographic effects is then calculated as equation 1 [24, 29, 32]:

$$L_H = L_T \times \frac{\cos \theta_z}{\cos \theta_i} \quad (1)$$

In the current study, the cosine method was applied regarding its simple and reliable functionality. The task was implemented by programming in interactive data language (IDL).

## 4.4. Data quality assessment

Existence of noisy bands (bad bands) in data causes inaccuracy in the resultant unmixing and classification maps. Briefly, a bad band refers to a band that has insignificant/inconsiderable or no information to be extracted [33, 34]. The effect of noise (N) on an image digital number (DN) at the  $i^{th}$  and  $j^{th}$  pixels is modeled as the summation of the true signal (S) and noise [11, 35, 36]:

$$DN_{i,j} = S_{i,j} + N_{i,j} \quad (2)$$

Consequently, if the noise significantly affects the images, the recorded value in the image pixels will be approximately equal to the noise amount, and the band will be indicated as a bad band. Signal to Noise Ratio (SNR) is one of the most effective indicators in the quality assessment of the hyperspectral images [33, 34, 37, 38]. Several image-based methods have been developed for the approximation of the image SNR. Most of these approaches are conducted through the comparison of the mean spectral response (representing the signal) to the standard deviation values (representing the image noise) [39, 40]. Accordingly, the mean to standard deviation method was applied to approximate the SNR of the Hyperion image in this work. In addition to the un-calibrated (1-7, 58-76, 225-242) and spectrally overlapping bands (57, 77), the bands with considerably lower SNR concerning to the adjacent bands were also marked as bad bands. Therefore, only the informative bands (178 out of total 242 bands) were selected for the unmixing process.

## 5. Unmixing

Hyperspectral imagery makes it possible to investigate the earth surface in more detail. It is, therefore, employed in a diversity of earth sciences, particularly in mineral exploration [1]. Mixed pixels are, however, a challenging problem in the hyperspectral data arising from the insufficient spatial resolution of the sensors or due to the combination of distinct materials into a microscopic mixture regardless of the ground resolution [3]. The radiance of a mixed pixel is a combination of the individual pure spectra of intimated materials in that pixel. Thus it is necessary to unmix the pixel spectra to determine the abundances fractions of each constituent or endmember [1, 41]. The linear mixture model (LMM) has been widely utilized in the development of unmixing algorithms due to its simplicity and acceptable functionality in many real datasets. According to this theory, the spectrum of a mixed pixel is a linear combination

of the endmember spectra weighted by their respective abundances [1, 42].

The standardized methods developed by analytical imaging and geophysics (AIG) [43, 44] was employed for unmixing the studied image (Figure 4). AIG is a stepwise algorithm, which is embedded in an ENVI platform. A data reduction procedure in both the spectral and spatial dimensions is applied through this methodology for data compression. The available endmembers are then identified using the N-dimensional visualization of the purest pixels, which are extracted from the pixel purity index (PPI) analysis. Finally, the distribution of the extracted endmembers is mapped with the use of the mixture tuned matched filtering (MTMF) method that maximizes the desired endmember signature and minimizes the background or undesired signal. The methodology is described in the next sections.

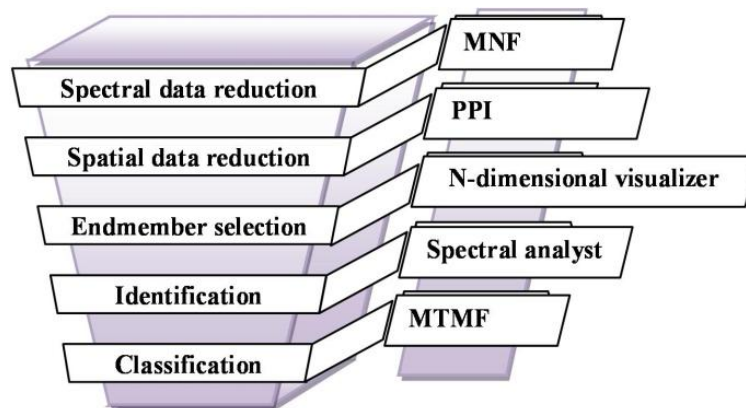


Figure 4. A Schematic diagram presenting standardized AIG hyperspectral analysis procedure.

### 5.1. Spectral data reduction

The MNF transformation is applied by AIG to reduce the band numbers. MNF is a useful tool to determine the inherent dimensionality of data with noise whitening. The lower order MNF bands (noise-dominated images) were discarded from the next processing steps [41, 43, 45]. Therefore, only the first 25 MNF bands were selected for further analysis in this study.

### 5.2. Spatial data reduction

Pixel purity index (PPI) is a process to find the most spectrally pure pixels (potential endmembers) in an image. Reflectance of the mixed pixels is then considered as a linear combination of the pure pixel spectra [41, 43, 45]. The recorded spectra is thought as points in an n-dimensional scatter plot, where n is the band number. The coordinates of the points in this

space are constructed from the spectral reflectance values in each band for a given pixel. The scatter plot of the pure pixels in the n-space is utilized to understand the spectral characteristics of the features in an image. In addition, this tool allows comparing not only the relationship between the data values in various bands but also the spatial distribution of the pixels in any area of the scatter plot. The distribution of the purest pixels is used to estimate the number of endmembers and their pure spectral signatures [43, 46, 47].

The purity index is computed by repeatedly projecting n-dimensional scatter plots on random unit vectors. The total counts when each pixel is marked as extreme (fall onto the ends of the unit vectors) are presented as an image. The purest pixels with the highest purity index values are the candidate endmembers. The spectrally similar

pure pixels which represented the same endmembers were then eliminated [41, 43, 45].

### 5.3. Visualization

Target spectra or spectrally pure pixels, representing compositionally distinct materials in the scene, were determined after the PPI computations. This implementation significantly reduces the pixels to be searched for mineralogical spectral recognition. The pure pixel vectors were, therefore, visualized in the n-dimensional space (selected MNF bands) to find and cluster spectrally similar pixels for defining the endmember signatures [45, 48].

In fact, all mixed pixels are placed inside a simplex formed by the endmembers as its vertices. The abundances are also under the non-negativity and sum to unity constraints. Therefore, if there are only two endmembers in the scene, the mixed pixels will fall in a line and the endmembers at the two ends of the line, and similarly, three endmembers fall inside a triangle, and so on. Thus the spectral characteristics of the endmembers and their abundances are intuitively discoverable by this geometric model [43, 46, 47]. The endmembers in the scene were defined by visual

inspection of the distribution of the pure pixels in 2-3-4-dimensional scatter plots, considering various MNF bands. The mean spectral profiles of defined clusters were then calculated as the target endmember signatures.

### 5.4. Spectral identification

Once the endmember spectra were extracted, the identification of their mineralogy was performed by matching them to the USGS reference spectra that are resampled to the Hyperion data [45, 46]. The spectral feature fitting (SFF) method was then applied to identify the corresponding minerals of each endmember. In addition, the consistency of the reference spectra and spectral profiles of endmembers were also visually verified in the SWIR range. This range of wavelength plays a vital role in discrimination among different minerals because minerals generally have obvious absorption features in this range (1.9-2.4  $\mu\text{m}$ ). This was resulted in the identification of five minerals including natrolite, analcime, opal, kaolinite, albite, whose spectral profiles are illustrated in Figure 5. The endmember signatures before the smile correction were also presented in this figure to show its effect in the VNIR region.

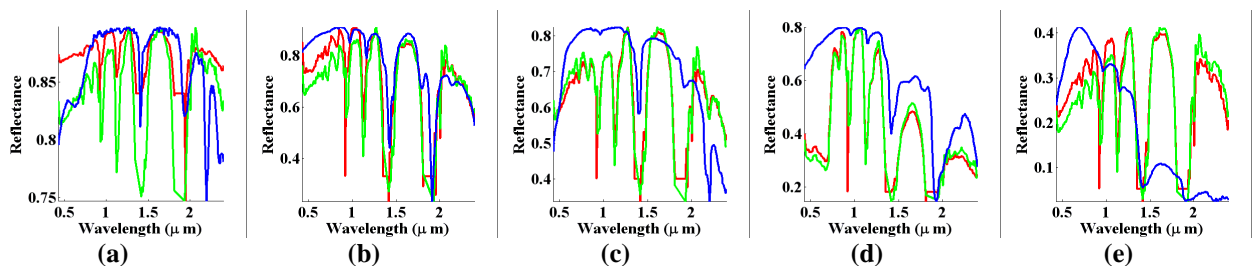


**Figure 5. Endmember spectral profile before (red) and after smile correction (green) along with the best matching reference spectra (blue) (a) natrolite, (b) opal, (c) analcime, (d) kaolinite, (e) albite.**

### 5.5. Classification

The mixture tuned matched filtering (MTMF) is a common technique used to map the endmember distributions. It uses an estimate of the background statistics to suppress the response of unknown background, while maximizing the response of the known endmember spectra. Prior knowledge about all background signatures is not needed in application of MTMF, and it, therefore, provides a more practical unmixing. In addition, this technique generates an infeasibility image for each endmember to prevent detection of false positives [46, 48-51]. The best mapping results correspond to the pixels with higher MF and lower infeasibility score [47, 49, 50].

MTMF was applied on both the smile corrected and uncorrected data of the studied area, and

resulted in a classification map of detected minerals based on their abundances in the image pixels. The pixels having higher infeasibility scores ( $>9$ ) were assigned as unclassified. The pixels infeasibility scores in the resulted MTMF maps varied from 1.8 up to 44.4. Examination of the different infeasibility scores implicated that the threshold 9 discards nearly all the unreliable estimates of the MF mapping results. The resulting mineralogical maps and the geological setting of the study area were presented in Figure 6. As implied from the final classification maps, the smile corrected data resulted in a more accurate classification.

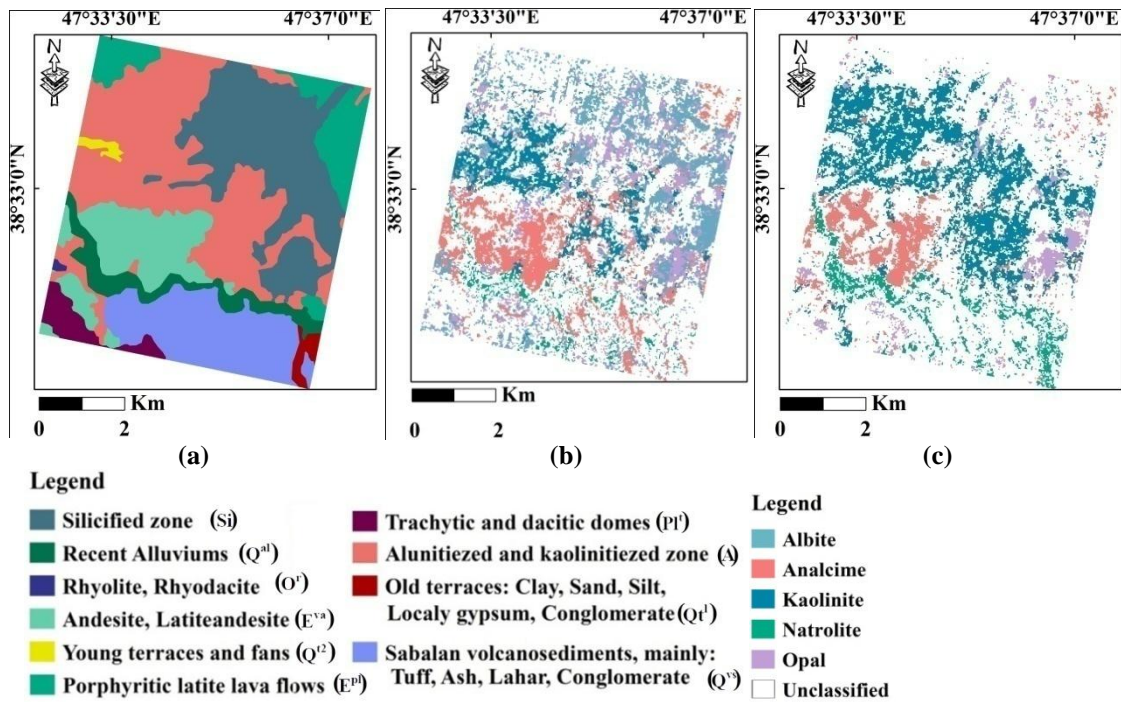


Figure 6. (a) Geological map of studied area, (b) and (c) Mineralogical maps before and (c) after smile correction, respectively.

### 6. Validation

The validation of the resultant maps of the smile corrected image was conducted using the geological setting and their constituent minerals. Therefore, the extension of the lithological units and rock types in the studied area was digitized from the 100 k geological map of the Lahroud sheet [52]. The intersection area of the resultant MTMF classification map and digitized lithological units (Figure 6a) was then computed in ArcGIS. The area of mineral subsections in

each lithological unit was divided by the total area of that unit. The results obtained are presented in

Table 1 and Figure 7. The total coverage of the lithological units in the studied area (from geological map [52]) and the area occupied by each mineral class at the MTMF map are presented in Figure 7.

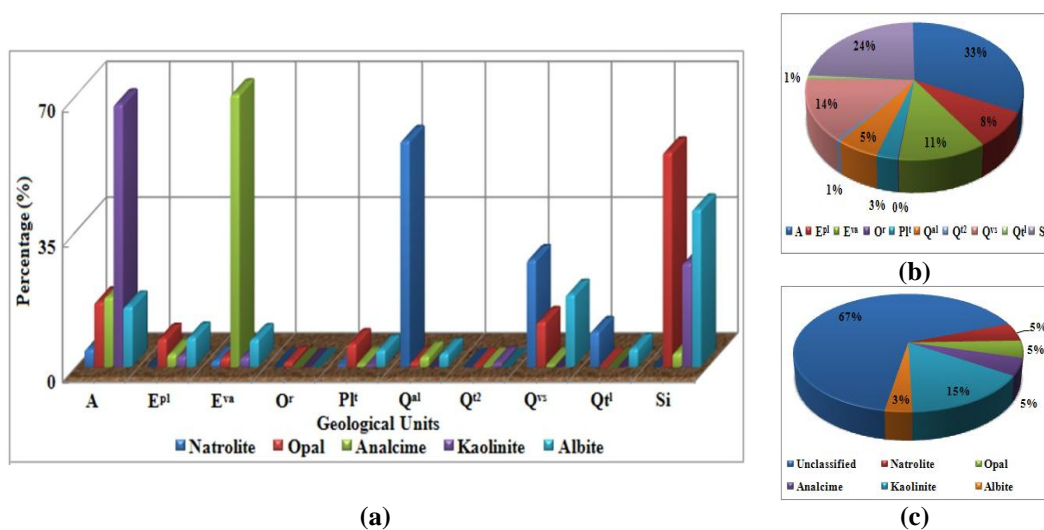


Figure 7. (a) Percentage of area covered by each mineral class in existed lithological units (digitized from [52]), and their coverages (b), (c) Coverage of extracted mineral at final MTMF map.

**Table 1. Quantitative comparison of coverage of minerals and lithological units in studied area in addition to the corresponding rock types in Figure 7.**

Symbol [52]	Description of geological units [52]	Area (%)	Coverage of minerals in lithological units (%)				
			Natrolite	Opal	Analcime	Kaolinite	Albite
A	Alunitiezed and kaolinitiezed zone	32.7	4.3	16.4	17.8	67.4	15.3
E <sup>pl</sup>	Porphyritic latite lava flows	8.3	0.0	7.0	3.0	2.6	7.3
E <sup>va</sup>	Andesite, Latiteandesite	11.3	1.3	2.2	72.2	2.3	6.9
O <sup>r</sup>	Rhyolite, Rhyodacite	0.1	0.0	1.0	0.0	0.0	0.0
Pl <sup>t</sup>	Trachytic and dacitic domes	2.7	0.3	5.6	0.7	0.4	4.1
Q <sup>al</sup>	Recent Alluviums	5.4	58.0	1.0	2.4	0.0	3.2
Q <sup>t2</sup>	Young terraces and fans	0.6	0.0	0.2	0.1	0.8	0.0
Q <sup>vs</sup>	Sabalan volcanosediments, mainly: Tuff, Ash, Lahar, Conglomerate	14.3	27.3	11.3	0.5	0.0	18.3
Qt <sup>l</sup>	Old terraces: Clay, Sand, Silt, Locally gypsum, Conglomerate	1.0	8.8	0.1	0.0	0.0	4.5
Si	Silicified zone	23.6	0.0	55.0	3.4	26.5	40.3

According to the results obtained, distribution of the detected minerals was strongly consistent to the geological setting indicated in the geological map of the region. Kaolinite was mostly mapped in the alunitiezed and kaolinitiezed alteration zones (67.4%), opal in the silicified zone (55%), natrolite in the recent alluviums (58%), analcime in the andesite, latiteandesite rocks (72.2%), and albite in most of the lithological units in the studied area, as expected. In addition, mineral occurrences in the respective rocks are reported in the map description based on the field studies.

**7. Results and discussion**

In this work, the effect of smile correction on a Hyperion scene for mineral mapping was surveyed, and, therefore, the “column mean adjusted in MNF space” method was exploited. The effect of correction was surveyed by investigating the unmixing results of the corrected and uncorrected image. Five minerals were then identified using the standardized AIG hyperspectral analysis procedure, and their abundance maps were generated by the MTMF approach. According to the geological setting, two alterations including the alunitiezed/kaolinitiezed and silicified zones dominantly occur in the region. These alterations were identified in the MTMF map through the distribution of the kaolinite and opal indicative minerals, respectively. Meanwhile, the detected clay minerals like kaolinite were lead to the existing of hydrothermal alterations, and they were irrelevant to the secondary clay minerals that are common in

sediments. Analcime bearing andesite, latite, and dacite rocks are also common rock types in the studied area, which were successfully reflected by analcime detection. Albite is common in most various volcanic and low-grade metamorphic rocks, and was mapped in most igneous outcrops in the region. Natrolite was dominantly mapped in the recent alluviums, which is acceptable according to its genesis and occurrence conditions as a member zeolite minerals. However, as implied by the classification maps, correcting the smile effect improved the distribution map slightly (uniform strips of mineral abundances on classification map), although did not seriously affect the spectra of the detected endmembers. Thus regarding the geological setting in the studied area and its sophisticated facieses, this work proved the efficiency of the Hyperion datasets in mineralogical mapping *after* application of the necessary pre-processings including smile correction. Regarding the obvious absorption features of most minerals in the SWIR region, performing the matching process in this region will improve the mineral detections.

**8. Conclusions**

The Hyperion scene of the Lahroud region, situated in the NW of Iran, was unmixed for mineral detection and alteration mapping. Accordingly, the necessary preprocessing steps were applied to the dataset to improve the image quality. A common error typically known to occur in the push-broom sensors like Hyperion is the spectral smile, while the existence of this effect is

not obvious on the individual Hyperion bands, evaluation of the smile indicators (MNF1 and band differential images), especially in the VNIR region, demonstrated the necessity of the smile correction. Thus pre-processing was conducted by performing the smile (column mean adjusted in MNF space), topographic (cosine method), and atmospheric correction (FLAASH); and data quality assessment (mean/standard deviation method) sequentially to increase the processing accuracy. In addition, the mapping results of the data without smile correction was investigated to evaluate the role of the smile correction in the resultant classification map.

The standardized AIG hyperspectral analysis was employed to extract the mineralogical and geological information of the studied area. The spectral unmixing of the Hyperion image resulted in the identification of five indicative minerals including natrolite, opal, analcime, kaolinite, and albite. Their spectral profiles were applied for generation of the classification map.

Examination of the final mineralogical map regarding the geological setting of the Lahroud region was conducted quantitatively. Therefore, the coverage of the extracted minerals was investigated in comparison to the location of the lithological units in ArcGIS. The results obtained implied the high consistency of the mineral distributions to the geological settings. Accordingly, kaolinite with the highest coverage in the alunitized and kaolinitized zone previously determined on the geological map [52] was defined as the representative of this alteration (67.4%). Similarly, opal is the representative of the silicified alteration with the coverage of 55% in this zone. The outcomes confirmed the efficiency of the applied approach in alteration mapping. However, as implied in the classification maps, correcting the smile effect resulted in a more accurate classification. Though the smile correction did not seriously affect the extracted endmembers signatures but caused some uniform strips of the minerals abundances that decreased the accuracy. The high consistency between the classification and geological maps of the studied area indicated the reliability of the proposed approach in the Hyperion data unmixing.

## References

[1]. Chang, C.I. (2007). *Hyperspectral Data Exploitation: Theory and Applications*, Wiley.  
[2]. Zadeh, M.H., Tangestani, M.H., Roldan, F.V. and Yusta, I. (2014). Sub-pixel mineral mapping of a

porphyry copper belt using EO-1 Hyperion data. *Advances in Space Research*. 53 (3): 440-451. Doi:10.1016/j.asr.2013.11.029.

[3]. Iordache, M-D., Bioucas-Dias, J.M. and Plaza, A. (2011). Sparse Unmixing of Hyperspectral Data. *IEEE Transactions on Geoscience and Remote Sensing*. 49 (6): 2014-2039. Doi:10.1109/tgrs.2010.2098413.

[4]. Goodenough, D.G., Dyk, A., Niemann, K.O., Pearlman, J.S., Hao, C., Tian, H., Murdoch, M. and West, C. (2003). Processing Hyperion and Ali for forest classification. *IEEE Transactions on Geoscience and Remote Sensing*. 41 (6): 1321-1331. Doi:10.1109/tgrs.2003.813214.

[5]. Mather, P.M. and Koch, M. (2011). Preprocessing of Remotely-Sensed Data. In: *Computer Processing of Remotely-Sensed Images: An Introduction*: 87-124, 4 Eds. John Wiley & Sons, Ltd, Chichester, UK.

[6]. Vesanto, V-H., Mottus, M., Heiskanen, J., Rautiainen, M. and Majasalmi, T. (2012). Atmospheric correction of a seasonal time series of Hyperion EO-1 images and red edge inflection point calculation. 4th Workshop on Hyperspectral Image and Signal Processing: Evolution in Remote Sensing (WHISPERS), Shanghai, pp. 1-4.

[7]. Cairns, B., Carlson, B.E., Ruoxian, Y., Lacin, A.A. and Oinas, V. (2003). Atmospheric correction and its application to an analysis of Hyperion data. *IEEE Transactions on Geoscience and Remote Sensing*. 41 (6): 1232-1244. Doi:10.1109/tgrs.2003.813134.

[8]. Kumar, C., Shetty, A., Raval, S., Champatiray, P.K. and Sharma, R. (2014). Sub-Pixel Mineral Mapping Using EO-1 Hyperion Hyperspectral Data. *The International Archives of the Photogrammetry, Remote Sensing and Spatial Information Sciences*, Hyderabad, India.

[9]. Oskouei, M.M. and Busch, W. (2008). A Geostatistically Based Preprocessing Algorithm for Hyperspectral Data Analysis. *GIScience & Remote Sensing*. 45 (3): 356-368. Doi:10.2747/1548-1603.45.3.356.

[10]. Poormirzaee, R. and Oskouei, M.M. (2010). Use of spectral analysis for detection of alterations in ETM data, Yazd, Iran. *Applied Geomatics*. 2 (4): 147-154. Doi:10.1007/s12518-010-0027-8.

[11]. Oskouei, M.M. (2010). Independent Component Analysis of Hyperion Data to Map Alteration Zones. *PFG*. 3: 179-189. Doi: 10.1127/1432-8364/2010/0048

[12]. Crósta, A.P., De Souza Filho, C.R., Azevedo, F. and Brodie, C. (2003). Targeting key alteration minerals in epithermal deposits in Patagonia, Argentina, using ASTER imagery and principal component analysis. *International Journal of Remote Sensing*. 24 (21): 4233-4240. Doi:10.1080/0143116031000152291.

- [13]. Dadon, A., Ben-Dor, E. and Karnieli, A. (2010). Use of Derivative Calculations and Minimum Noise Fraction Transform for Detecting and Correcting the Spectral Curvature Effect (Smile) in Hyperion Images. *IEEE Transactions on Geoscience and Remote Sensing*. Doi:0.1109/TGRS.2010.2040391.
- [14]. Datt, B., Mccicar, T.R., Van Niel, T.G., Jupp, D.L.B. and Pearlman, J.S. (2003). Preprocessing EO-1 Hyperion hyperspectral data to support the application of agricultural indexes. *IEEE Transactions on Geoscience and Remote Sensing*. 41 (6): 1246-1259. Doi:10.1109/tgrs.2003.813206.
- [15]. Yaokai, L., Tianxing, W., Lingling, M. and Ning, W. (2014). Spectral Calibration of Hyperspectral Data Observed From a Hyperspectrometer Loaded on an Unmanned Aerial Vehicle Platform. *IEEE Journal of Selected Topics in Applied Earth Observations and Remote Sensing*. 7 (6): 2630-2638. Doi:10.1109/jstars.2014.2329891.
- [16]. Ceamanos, X. and Doute, S. (2010). Spectral Smile Correction of CRISM/MRO Hyperspectral Images. *IEEE Transactions on Geoscience and Remote Sensing*. 48 (11): Doi:10.1109/tgrs.2010.2064326.
- [17]. Griffin, M.K. and Burke, H-H.K. (2003). Compensation of Hyperspectral data for atmospheric effects. *Lincoln Laboratory Journal*. 14 (1): 29-53.
- [18]. Jinguo, Y. and Zheng, N. (2008). Evaluation of atmospheric correction using FLAASH. *International Workshop on Earth Observation and Remote Sensing Applications (EORSA)*, Beijing. pp. 1-6. Doi: 10.1109/EORSA.2008.4620341.
- [19]. Goetz, A.F.H. (2009). Three decades of hyperspectral remote sensing of the Earth: A personal view. *Remote Sensing of Environment*. 113 (1): S5-S16. Doi:10.1016/j.rse.2007.12.014.
- [20]. Borengasser, M. (2015). *Hyperspectral Remote Sensing: Principles and Applications*, Second Edition, CRC Press.
- [21]. Kruse, F.A. (2004). Comparison of ATREM, ACORN, and FLAASH Atmospheric Corrections using Low-Altitude AVIRIS Data of Boulder, Colorado. 13<sup>th</sup> JPL Airborne Geoscience Workshop, Pasadena, CA.
- [22]. Li, C. (2009). Remote Sensing Image Based Analysis on Present Land Utilization of Chongqing Area. *Journal of Geography and Geology*. 1 (1): Doi:10.5539/jgg.v1n1p20.
- [23]. Singh, S. and Talwar, R. (2013). A Systematic Survey on Different Topographic Correction Techniques for Rugged Terrain Satellite Imagery. *International Journal of Electronics & Communication Technology (IJECT)*. 4 (5): 14-18.
- [24]. Vanonckelen, S., Lhermitte, S., Balthazar, V. and Van Rompaey, A. (2014). Performance of atmospheric and topographic correction methods on Landsat imagery in mountain areas. *International Journal of Remote Sensing*. 35 (13): 4952-4972. Doi:10.1080/01431161.2014.933280.
- [25]. Tokola, T., Sarkeala, J. and Van Der Linden, M. (2001). Use of topographic correction in Landsat TM-based forest interpretation in Nepal. *International Journal of Remote Sensing*. 22 (4): 551-563. Doi:10.1080/01431160050505856.
- [26]. Riano, D., Chuvieco, E., Salas, J. and Aguado, I. (2003). Assessment of different topographic corrections in landsat-TM data for mapping vegetation types (2003). *IEEE Transactions on Geoscience and Remote Sensing*. 41 (5): 1056-1061. Doi:10.1109/tgrs.2003.811693.
- [27]. Richter, R., Kellenberger, T. and Kaufmann, H. (2009). Comparison of Topographic Correction Methods. *Remote Sensing*. 1 (3): 184-196. Doi:10.3390/rs1030184.
- [28]. Ediriweera, S., Pathirana, S., Danaher, T., Nichols, D. and Moffiet, T. (2012). Impact of Different Topographic Corrections on Prediction Accuracy of Foliage Projective Cover (Fpc) in a Topographically Complex Terrain. *ISPRS Annals of Photogrammetry, Remote Sensing and Spatial Information Sciences*. I-7 123-128. Doi:10.5194/isprsannals-I-7-123-2012.
- [29]. Gao, M-L., Zhao, W-J., Gong, Z-N., Gong, H-L., Chen, Z. and Tang, X-M. (2014). Topographic Correction of ZY-3 Satellite Images and Its Effects on Estimation of Shrub Leaf Biomass in Mountainous Areas. *Remote Sensing*. 6 (4): 2745-2764. Doi:10.3390/rs6042745.
- [30]. Meyer, P., Itten, K.I., Kellenberger, T., Sandmeier, S. and Sandmeier, R. (1993). Radiometric corrections of topographically induced effects on Landsat TM data in an alpine environment. *ISPRS Journal of Photogrammetry and Remote Sensing*. 48 (4): 17-28. Doi:10.1016/0924-2716(93)90028-1.
- [31]. Colby, J.D. and Keating, P.L. (1998). Land cover classification using Landsat TM imagery in the tropical highlands: The influence of anisotropic reflectance. *International Journal of Remote Sensing*. 19 (8): 1479-1500. Doi:10.1080/014311698215306.
- [32]. Wu, J., Bauer, M.E., Wang, D. and Manson, S.M. (2008). A comparison of illumination geometry-based methods for topographic correction of QuickBird images of an undulant area. *ISPRS Journal of Photogrammetry and Remote Sensing*. 63 (2): 223-236. Doi:10.1016/j.isprsjprs.2007.08.004.
- [33]. Chein, I.C., Qian, D., Tzu-Lung, S. and Althouse, M.L.G. (1999). A joint band prioritization and band-decorrelation approach to band selection for hyperspectral image classification. *IEEE Transactions on Geoscience and Remote Sensing*. 37 (6): 2631-2641. Doi:10.1109/36.803411.

- [34]. Sefat, A.A.D. (2007) - Application of Hyperspectral Data for Forest Stand Mapping. *Iranian Journal of Natural Resources*. 59 (4): 831-841.
- [35]. Corner, B.R., Narayanan, R.M. and Reichenbach, S.E. (2003). Noise estimation in remote sensing imagery using data masking. *International Journal of Remote Sensing*. 24 (4): 689-702. Doi:10.1080/01431160210164271.
- [36]. Petropoulos, G.P., Arvanitis, K. and Sigrimis, N.A. (2012) - Hyperion hyperspectral imagery analysis combined with machine learning classifiers for land use/cover mapping. *Expert Systems with Applications*. 39: 3800-3809.
- [37]. Pearlman, J., Segal, C., Liao, L., Carman, S., Folkman, M., Browne, B., Ong, L. and Ungar, S. (2000). Development and operations of the eo-1 Hyperion imaging spectrometer. *Proceeding of SPIE 4135, Earth Observing Systems*. 243: 243-254. Doi:10.1117/12.494251.
- [38]. Gersman, R., Ben-Dor, E., Beyth, M., Avigad, D., Abraha, M. and Kibreab, A. (2007). Hyperspectral Remote Sensing As A Tool For Geological Exploration – Examples From The Northern DANAKIL DEPRESSION, ERITREA. 5th EARSeL Workshop on Imaging Spectroscopy, Bruges, Belgium.
- [39]. Atkinson, P.M., Sargent, I.M., Foody, G.M. and Williams, J. (2007). Exploring the Geostatistical Method for Estimating the Signal-to-Noise Ratio of Images. *Photogrammetric Engineering & Remote Sensing*. 73 (7): 841-850. Doi:10.14358/pers.73.7.841.
- [40]. Hruska, R., Mitchell, J., Anderson, M. and Glenn, N.F. (2012). Radiometric and Geometric Analysis of Hyperspectral Imagery Acquired from an Unmanned Aerial Vehicle. *Remote Sensing*. 4 (12): 2736-2752. Doi:10.3390/rs4092736.
- [41]. Bioucas-Dias, J.M., Plaza, A., Dobigeon, N., Parente, M., Du, Q., Gader, P. and Chanussot, J. (2012). Hyperspectral Unmixing Overview: Geometrical, Statistical, and Sparse Regression-Based Approaches. *IEEE Journal of Selected Topics in Applied Earth Observations and Remote Sensing*. 5 (2): 354-379. Doi:10.1109/jstars.2012.2194696.
- [42]. Nascimento, J.M.P. and Bioucas-Dias, J.M. (2012). Hyperspectral Unmixing Based on Mixtures of Dirichlet Components. *IEEE Transactions on Geoscience and Remote Sensing*. 50 (3): 863-878. Doi:10.1109/tgrs.2011.2163941.
- [43]. Kruse, F.A., Huntington, J.H. and Green, R.O. (1996). Results from the 1995 AVIRIS Geology Group Shoot. 2nd International Airborne Remote Sensing Conference and Exhibition: Technology, Measurement & Analysis, Environmental Research Institute of Michigan, Ann Arbor, San Francisco, California, USA, pp. I-211 - I-220.
- [44]. Kruse, F.A., Boardman, J.W. and Huntington, J.F. (2003). Comparison of airborne hyperspectral data and EO-1 Hyperion for mineral mapping. *IEEE Transactions on Geoscience and Remote Sensing*. 41 (6): 1388-1400. Doi:10.1109/tgrs.2003.812908.
- [45]. Vaughan, R.G., Hook, S.J., Calvin, W.M. and Taranik, J.V. (2005). Surface mineral mapping at Steamboat Springs, Nevada, USA, with multi-wavelength thermal infrared images. *Remote Sensing of Environment*. 99 (1-2): 140-158. Doi:10.1016/j.rse.2005.04.030.
- [46]. Kruse, F.A. (2003). Preliminary Results - Hyperspectral mapping of coral reef systems using EO-1 Hyperion, Buck Island, U.S. Virgin Islands. 12th JPL Airborne Geoscience Workshop, Pasadena, California. pp. 157 - 173.
- [47]. Ahmad, F. (2012). Pixel Purity Index Algorithm and n-Dimensional Visualization for ETM+ Image Analysis: A Case of District Vehari. *Global Journal of Human Social Science Arts & Humanities*. 12 (15): 76-82.
- [48]. Chabrilat, S., Goetz, A.F.H., Krosley, L. and Olsen, H.W. (2002) - Use of hyperspectral images in the identification and mapping of expansive clay soils and the role of spatial resolution. *Remote Sensing of Environment*. 82 (2-3): 431-445. Doi:10.1016/s0034-4257(02)00060-3.
- [49]. Mitchell, J.J. and Glenn, N.F. (2009). Subpixel abundance estimates in mixture-tuned matched filtering classifications of leafy spurge (*Euphorbia esula* L). *International Journal of Remote Sensing*. 30 (23): 6099-6119. Doi:10.1080/01431160902810620.
- [50]. Wen, X-P., Yang, X-F. and Hu, G-D. (2009). Hyperspectral Remote Sensing Data Mining Using Multiple Classifiers Combination. *Data Mining and Knowledge Discovery in Real Life Applications*, Ponce, J., Karahocas, A., (Eds.), In-Teh, Vienna, Austria.
- [51]. Molan, Y.E., Refahi, D. and Tarashti, A.H. (2014). Mineral mapping in the Maherabad area, eastern Iran, using the HyMap remote sensing data. *International Journal of Applied Earth Observation and Geoinformation*. 27: 117-127. Doi:10.1016/j.jag.2013.09.014.
- [52]. Ghandchi, M., Afsharian, A. and Chaichi Z. (1991). 1:100000 geological map of lahrud sheet. Geological Survey of Iran.

## نقش تصحیح انحنای طیفی در تشخیص کانی‌ها در داده‌های هایپریون

مجید محمدی اسکویی\* و سولماز بابکان

دانشکده مهندسی معدن، دانشگاه صنعتی سهند، ایران

ارسال ۲۰۱۵/۱۰/۱۴، پذیرش ۲۰۱۶/۱/۱۱

\* نویسنده مسئول مکاتبات: mohammady@sut.ac.ir

---

### چکیده:

هدف از این مطالعه تشخیص کانی‌های اصلی در یک بخش از تصویر هایپریون منطقه لاهرود واقع در شمال غربی ایران است. نظیر اغلب سنجنده‌های پوشش بروم، در تصاویر هایپریون نیز خطای حاصل از انحنای طیفی مشهود است. این اثر باعث ایجاد یک جابجایی طول موجی در جهت عمود بر حرکت سنجنده شده و به این ترتیب انرژی ثبت شده برای پیکسل‌ها در باندهای مختلف تغییر می‌یابد. در این مطالعه از روش «میانگین متوازن شده ستونی در فضای MNF» برای کاهش خطای انحنای طیفی و افزایش صحت پردازش استفاده شد. این عمل قبل از تصحیحات اتمسفری و توپوگرافی انجام گرفت. توزیع کانی‌ها توسط روش پردازش داده‌های هایپراسپکترال استاندارد ارائه شده توسط AIG تعیین و نقشه‌های فراوانی آن‌ها ترسیم شد. جداسازی طیفی داده‌ها منتج به تشخیص پنج کانی معرف اوپال، ناترولیت، آنالسیم، کائولینیت و آلبیت شد که در ادامه فراوانی طیف‌های آن‌ها در تصویر مورد مطالعه محاسبه شد. مقایسه نتایج حاصل از پردازش داده‌ها در دو حالت (با و بدون تصحیح انحنای طیفی)، نشان از تأثیر مثبت تصحیح مورد بحث بر عملکرد الگوریتم طبقه‌بندی در تصویر هایپریون داشت. اعتبارسنجی کمی نقشه توزیع کانی‌ها بر اساس مقایسه با نقشه و گزارش‌های زمین‌شناسی منطقه صورت گرفت. به این منظور مناطق پوششی هر کدام از کانی‌ها در محیط ArcGIS و تطابق منطقی آن‌ها با رخنمون‌های سنگی بررسی شد که نشانگر همبستگی بالایی است. با توجه به این رابطه منطقی بین رخنمون‌ها و کانی‌های شناخته شده در داخل آن‌ها، کاربرد روش مورد بحث در شناسایی روند کانی‌سازی در اکتشافات معدنی البته با انجام تصحیحات لازم توصیه می‌شود.

**کلمات کلیدی:** داده‌های هایپریون، روش پردازش استاندارد داده‌های هایپراسپکترال، تصحیح انحنای طیفی، نقشه‌برداری کانی‌ها.

---